Alteration of fossil-bearing shale (Autun Basin, France; Permian), part I: Characterizing iron speciation and its vulnerability to weathering by combined use of Mössbauer spectroscopy, X-ray diffraction, porosimetry and permeability measurements

Giliane P. Odin, Thomas Cabaret, Jean Didier Mertz, Beatriz Menendez, Laetitia Etienne, Alain Wattiaux, Véronique Rouchon

Annales de Paléontologie 101 (2015) 75–85

Disponible en ligne sur
ScienceDirect
www.sciencedirect.com

Elsevier Masson France
EM|consulte
www.em-consulte.com

Original article

Alteration of fossil-bearing shale (Autun Basin, France; Permian), part I: Characterizing iron speciation and its vulnerability to weathering by combined use of Mössbauer spectroscopy, X-ray diffraction, porosimetry and permeability measurements

Dégradation de schistes argileux fossilifères (bassin d'Autun, France, Permien), partie I : caractérisation de la spéciation et de la réactivité du fer par spectrométrie Mössbauer, diffraction des rayons X, porosimétrie et mesure de perméabilité

Giliane P. Odin[a,b], Thomas Cabaret[a], Jean Didier Mertz[a,c], Beatriz Menendez[d], Laetitia Etienne[e], Alain Wattiaux[e], Véronique Rouchon[a,*]

[a] *Centre de Recherche sur la Conservation (CRC, USR 3224), Sorbonne Universités, Muséum national d'Histoire naturelle, Ministère de la Culture et de la Communication, CNRS ; CP21, 36, rue Geoffroy-Saint-Hilaire, 75005 Paris, France*
[b] *Centre de Recherche sur la Paléobiodiversité et les Paléoenvironnements (CR2P, UMR 7207), Sorbonne Universités, Muséum national d'Histoire naturelle, Université Pierre et Marie Curie, CNRS, CP 38, 8, rue Buffon, 75005 Paris, France*
[c] *Laboratoire de Recherche des Monuments Historiques (LRMH), 29, rue de Paris, 77420 Champs-sur-Marne, France*
[d] *Géosciences et Environnement Cergy (GEC), Université de Cergy-Pontoise, 5 mail Gay-Lussac, rue d'Eragny, Neuville-sur-Oise, 95031 Cergy-Pontoise cedex, France*
[e] *CNRS, Université de Bordeaux, ICMCB, UPR9048, 87, avenue du Docteur Schweitzer, 33600 Pessac, France*

ARTICLE INFO

Article history:
Received 5 September 2014
Accepted 7 January 2015
Available online 9 February 2015

Keywords:
Shale
Fossil
Pyrite
Autun Basin
Oxidation
Iron
Sulfide
Clay
Mössbauer

ABSTRACT

Fossil-bearing shale specimens that include sulfides in their compositions are chemically reactive and sometimes also mechanically fragile. This decay is often related to iron sulfate efflorescence resulting from the oxidation of sulfide compounds. The processes underlying these degradations are poorly known, thus impeding the elaboration of curative or preventive treatments. The present contribution aims to identify the origin of museum specimen alterations. It focuses on the Flouest collection housed at the Muséum national d'Histoire naturelle (MNHN, Paris, France) and originating from the Autun Basin (Saône-et-Loire, France; Permian). To evaluate the alteration of MNHN specimens, it appeared necessary to compare their composition with that of unaltered shale so as to identify chemical changes occurring during ageing. Therefore new material was collected in the Autun Basin, among others on the locality of Muse that corresponds to the same lithostratigraphic unit than that of the MNHN specimens. The present article focuses on the combined use of X-ray diffraction and Mössbauer spectrometry for characterizing the speciation and reactivity of iron within the shale matrix. Crystalline pyrite was evidenced by X-ray diffraction (XRD) on one sample only and elemental analysis showed that iron is present in large excess with respect to sulfur. Iron sulfide, if present, involves a minor fraction of iron. A more complete characterization of iron-bearing phases was achieved with Mössbauer measurements, showing that a great part of iron, between approx. 25% and 65%, corresponds to iron(II) incorporated in clay minerals (illite and vermiculite were detected by XRD). Similar percentages of these iron(II) signatures were found for MNHN specimens and new shale samples, suggesting that iron(II) present in clays is not affected by ageing. This point is complementary highlighted by porosity and permeability measurements showing that the pore size distribution of the samples originating from Muse is mostly unimodal and narrow (average radius below 10 nm). As a result, the shale is poorly permeable to water and almost fully impermeable to oxygen. This might explain the poor reactivity of iron(II) during ageing. Iron(III)-bearing phases were also identified. On new shale samples, they exclusively involve clay minerals. On MNHN specimens, poorly crystallized iron(III)

* Corresponding author.
E-mail addresses: giliane.odin@mnhn.fr (G.P. Odin), tcabaret@yahoo.fr (T. Cabaret), jean-didier.mertz@culture.gouv.fr (J.D. Mertz), beatriz.menendez@u-cergy.fr (B. Menendez), etiennel@icmcb-bordeaux.cnrs.fr (L. Etienne), wattiaux@icmcb-bordeaux.cnrs.fr (A. Wattiaux), rouchon@mnhn.fr (V. Rouchon).

http://dx.doi.org/10.1016/j.annpal.2015.01.002

sulfates are additionally observed. The presence of iron(III) oxyhydroxides appeared unlikely. The change of iron speciation provoked by the alteration of the matrix also mainly corresponds to the emergence of more or less crystallized iron(III) sulfates probably formed though iron sulfide oxidation. These phases however remain in the inner part of shale and cannot account for the large efflorescence of iron(II) sulfates observed nearby the fossil.

Mots clés :
Schiste argileux
Fossile
Pyrite
Bassin d'Autun
Oxydation
Fer
Sulfure
Argile
Mössbauer

RÉSUMÉ

Les schistes argileux fossilifères qui incluent des sulfures dans leur composition sont chimiquement réactifs et deviennent aussi parfois fragiles mécaniquement. Ces dégradations sont souvent liées à des efflorescences de sulfates de fer(II) résultant de l'oxydation de produits sulfurés. Les mécanismes sous-jacents à ces dégradations sont généralement peu connus, ce qui limite l'élaboration de traitements curatifs ou préventifs. Ce travail vise à identifier l'origine des dégradations observées sur les spécimens de collections, en particulier ceux de la collection Flouest qui provient du bassin d'Autun (Saône-et-Loire, France, Permien) et est aujourd'hui conservée au Muséum national d'Histoire naturelle (MNHN). Pour évaluer la dégradation des spécimens MNHN, il est apparu nécessaire de comparer leur composition à celle de schistes argileux non altérés, de manière à mettre en évidence les changements de composition chimique. C'est pourquoi du matériel neuf a été prélevé dans le bassin d'Autun, entre autres sur le site de Muse qui correspond à la même unité lithostratigraphique que celle des spécimens MNHN. Cet article porte plus spécifiquement sur l'utilisation conjointe de la diffraction des rayons X et de la spectrométrie Mössbauer pour caractériser la spéciation et la réactivité du fer dans la matrice argileuse. De la pyrite cristalline a été mise en évidence par diffraction des rayons X (DRX) sur seulement un échantillon et les analyses élémentaires montrent que le fer est présent en large excès par rapport au soufre. Le sulfure de fer, si présent, ne peut donc impliquer qu'une fraction mineure de fer. Une caractérisation plus complète des phases de fer a été obtenue par des mesures Mössbauer qui ont montré qu'une majeure partie du fer, entre environ 25 % et 65 %, correspond à du fer(II) présent dans les minéraux argileux (de l'illite et de la vermiculite ont été identifiées par DRX). Des pourcentages similaires de ces signatures de fer(II) ont été mesurés sur les spécimens MNHN et sur le nouveau matériel prélevé, ce qui suggère que le fer(II) présent dans les argiles n'est pas affecté par le vieillissement. Un éclairage complémentaire de ce point est donné par les mesures de porosité et de perméabilité, qui montrent, dans les échantillons de Muse, une distribution de pores unimodale et étroite (rayon moyen inférieur à 10 nm). De ce fait, le schiste argileux est très peu perméable à l'eau et presqu'entièrement imperméable à l'air, ce qui explique la faible réactivité du fer(II) pendant le vieillissement. Les phases de fer(III) ont également été identifiées. Sur le matériel neuf, elles correspondent exclusivement à des minéraux argileux. Sur les spécimens MNHN, on observe de plus des sulfates de fer(III) peu cristallisés. La présence d'oxy-hydroxydes de fer paraît peu probable. Les changements de spéciation du fer provoqués par la dégradation de la matrice correspondent donc principalement à l'émergence de sulfates de fer(III) plus ou moins cristallisés probablement formés par l'oxydation de sulfures de fer. Ces phases restent cependant dans la partie interne du schiste et ne permettent pas d'expliquer des larges efflorescences de sulfates de fer(II) qui apparaissent près des fossiles.

1. Introduction

The Autun Basin (Saône-et-Loire, France; Permian), the stratigraphy of which is well documented (Chateauneuf et al., 1980; Elsass Damon, 1977; Marteau, 1983), was the place of mining activity until the 60's (Chabard and Passaqui, 2006). It has thus provided numerous fossils and many of them can be found in Natural History Museum collections. Today all mines are flooded but many outcrops remain accessible in the Basin, still raising a significant paleontological interest. This is in particular the case of the site of Muse that was re-opened in 2010 for paleontological fieldwork (Gand et al., 2010).

The collections of the Muséum National d'Histoire Naturelle, Paris (MNHN) comprise several specimens collected in the "Autunian" of the Autun Basin in the 19th century. Some of them, such as those of the Flouest collection, are today severely damaged by iron sulfate efflorescence (Rouchon et al., 2012). It often underlines the fossil (Fig. 1a) and induces flaking (Fig. 1b,c). These degradations arouse several questions dealing with the cause of damage. In particular, is it due to the intrinsic composition of shale? Does it involve oxygen and/or humidity? Which are the most sensitive compounds involved?

Pyrite decay is often believed to be the cause of damage. Pyrite is an iron sulfide of chemical composition FeS_2 that is well known for its poor stability in ambient and humid conditions, leading to iron sulfate efflorescence (Howie, 1977; Jambor et al., 2000; Rosso and Vaughan, 2006). However the occurrence of pyrite in the Autun Basin shale is not obvious. The shale has a dark color and does not show pyrite-like crystals obviously noticeable by naked eye or under the stereomicroscope. Moreover, as the shale is rich in organic matter and was used in the past to produce oil and ammonium sulfate, it may contain some proportion of organic sulfides that could be reactive as well.

There is obviously an evolution of shale material after excavation, when it is transferred from a wet and low oxygen environment to ambient conditions. This evolution, associated to weathering phenomena, is not *stricto sensu* considered as damage unless it alters the appearance of the fossil (efflorescence) or its integrity (flaking).

This work was undertaken to better understand the damage observed on fossil-bearing shale, such as those of the Flouest collection. For this purpose, it was found necessary to follow the evolution of shale material after excavation by a large panel of techniques. As iron sulfates are the major degradation products, we mostly used analytical techniques that enable iron and sulfur characterization. This approach is a prerequisite for identifying weathering and damaging phenomena. It is expected to help in defining appropriate preservation conditions for damaged specimens, and also in

understanding the risk of damage related to similar paleontological material that is currently excavated.

This study is organized in three parts. The first part, reported in the present article, aims to identify iron-bearing phases associated to the shale matrix. The objective is to estimate the ability of iron to undergo chemical reactions within the matrix. For this purpose, X-ray diffraction (XRD), Mössbauer spectrometry (MS), porosimetry and permeability measurements were undertaken.

The two other parts deal with (i) the use of sulfur K-edge XANES spectroscopy to monitor sulfur speciation in shale and (ii) the reproduction on new material of the damage observed on MNHN specimens. They will be reported in forthcoming articles.

2. Samples and geological settings

2.1. Shale fraction of fossil specimens from the Flouest collection

Three specimens (MNHN.F.6889, MNHN.F.6891 and MNHN.F.6892) from the Flouest collection (MNHN) were chosen for analysis because they present typical degradation observed in that collection (Fig. 1). These specimens originate from the locality of "Le Ruet", in the Autun Basin and jointly entered the Museum collection in 1865. They are currently stored in the same drawer, in a room with no air conditioning, which variations in temperature and humidity were previously reported (Odin et al., 2014).

Identification and conservation report of these fossils can be found elsewhere (Rouchon et al., 2012). The three specimens are severely damaged by crystalline efflorescence that is related to iron(II) sulfates (rozenite, $Fe^{II}SO_4$, $4H_2O$ and szomolnokite $Fe^{II}SO_4$, H_2O) with some minor proportion of iron(III) sulfates (jarosite, $KFe^{III}_3(SO_4)_2(OH)_6$, in the case of sample 6891 and ferricopiapite, $Fe^{III}_{2/3}Fe^{III}_4(SO_4)_6(OH)_2{\cdot}20H_2O$, in the case of sample 6889). This efflorescence has mainly grown near or on the fossil. The shale portions thus appear in relatively fair condition and were sampled on the back side of the specimens. They are hereafter referred to as 6889, 6891 and 6892.

2.2. Newly excavated shale samples

2.2.1. Shale samples from the locality of Muse

In order to reproduce damage in laboratory conditions, it was intended to sample new shale material with petrographic characteristics similar than those of damaged specimens. Unfortunately the mine of Le Ruet (Tavernay, Saône-et-Loire, France), which probably yielded the MNHN specimens is no longer accessible. We opted for an alternative outcrop with the same lithostratigraphic unit (i.e. the bedding of Muse, "Autunian" of the Autun Basin): the outcrop of Muse (Dracy Saint-Loup, Saône-et-Loire, France), located approximately 6 km from the locality of Le Ruet, was therefore chosen. This choice was also motivated by the fact that the site is currently open for paleontological fieldwork (Gand et al., 2010).

The "Autunian" of the Muse outcrop comprises several layers, the most famous of which is commonly called the "Muse fish layer" and hereafter referred to as *Muse FL* (Fig. 2a,b). This layer (Late carboniferous-lower Permian of the Autun Basin) is located at the base of the bedding of Muse and above a pebble layer (Sandstones of Lally). Since the 19th century, the *Muse FL* yielded hundreds of *Actinopterygii* specimens (mostly Aeduellidae) now spread in many museum collections and in various conditions of conservation. Specimens found in this layer are of exceptionnal preservation. They are currently collected for research and exhibition purposes. A better knowledge of the *Muse FL* composition and stability versus time will certainly help monitoring the future preservation of *Actinopterygii* specimens in Museum collections.

The layers above the *Muse FL*, hereafter referred to as *Muse*, are also of paleontological interest although the fossils they contain are less spectacular: they mainly consist of botanical remains (palynomorphs, macro-remains), "cockroachoid" insects (Stem-Dictyoptera) and crustaceans (Ostracods). Some samples were

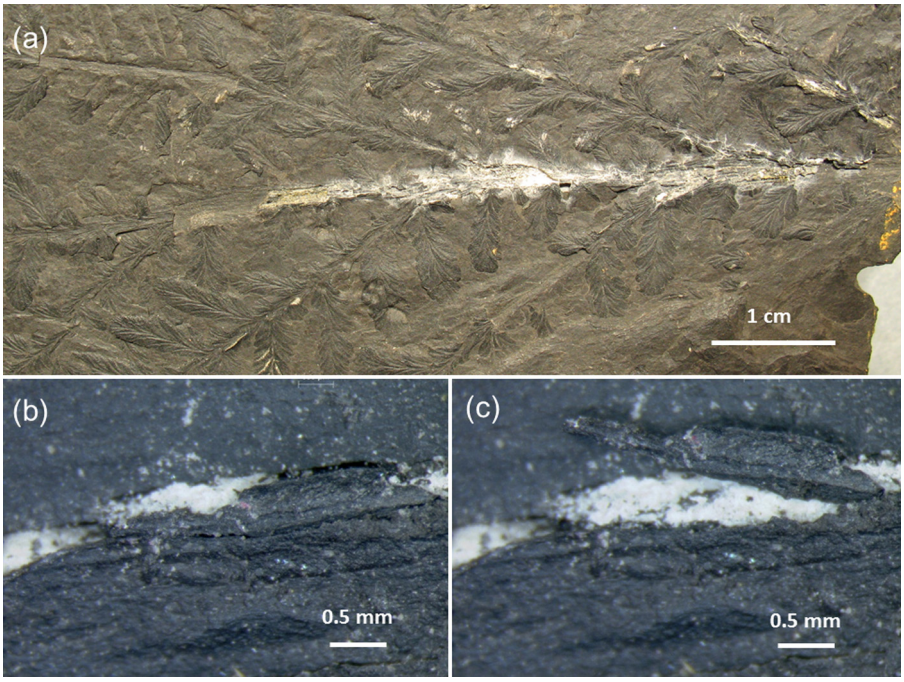

Fig. 1. Example of damage observed on the specimens of the Flouest collection, MNHN. Example of efflorescence formed in the proximity of the fossil (a), specimen MNHN.F.6891; example of an efflorescence growth (b) that has provoked the detachment of a flake (c) on the specimen MNHN.F.6889.
Exemples de dommages observés sur les spécimens de la collection Flouest, MNHN. Exemple d'efflorescence formée à proximité du fossile (a), spécimen MNHN.F.6891 ; exemple d'efflorescence (b) qui a provoqué le détachement d'une écaille (c) sur le spécimen MNHN.F.6889.

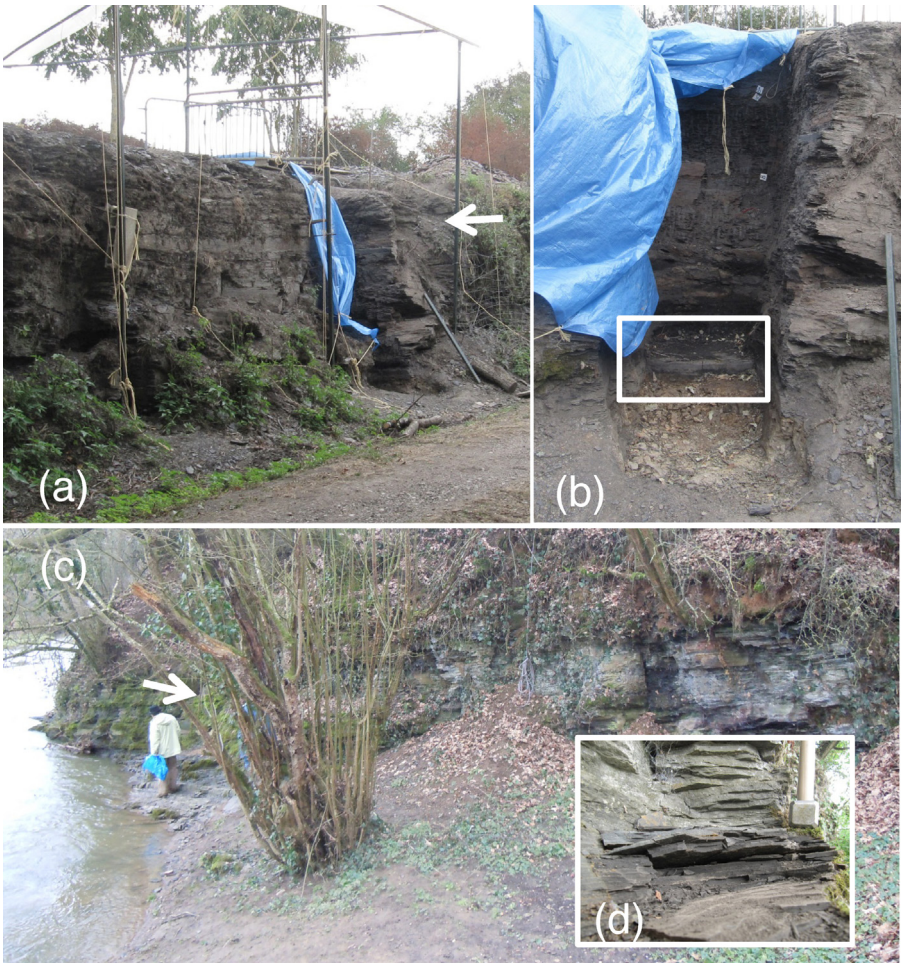

Fig. 2. Embankments of the localities of Muse and Surmoulin. (a) locality of Muse, general view from the track, location of Muse samples (white arrow); (b) location of *Muse FL* samples (white rectangle); (c) locality of Surmoulin, general view, location of Surmoulin samples (white arrow); (d) detail of Surmoulin samples.
Talus des sites de Muse et Surmoulin. (a) site de Muse, vue générale du chemin montrant l'emplacement des échantillons Muse (flèche blanche) ; (b) emplacement de la couche Muse FL *(rectangle blanc) ; (c) site de Surmoulin, vue générale et emplacement des échantillons Surmoulin (flèche blanche) ; (d) détail des échantillons Surmoulin.*

additionnally taken in these layers, approx. 1–2 meters above the *Muse FL* (Fig. 2a). They are hereafter referred to as *Muse* samples.

2.2.2. Shale samples from the locality of Surmoulin

In a previous study (Odin et al., 2014), samples were taken from different outcrops of the Autun Basin for artificial ageing experiments. Among these, the samples from the Surmoulin layer (outcrop of Surmoulin, Dracy Saint-Loup, Saône-et-Loire, France) were the most reactive: they showed large calcium sulfate efflorescence and substantial mechanical damage versus artificial ageing. It was also found relevant to work on this material, hereafter referred to as *Surmoulin.*

2.2.3. Cautions taken during shale sampling

The site of Muse is located in the embankment of a road (Fig. 2a) and that of Surmoulin in the embankment of a river (Fig. 2c, d), meaning that samples were collected close to the surface and were also subjected to weathering. When split, they showed orange rust-colored areas, confirming that they had been partially exposed to weathering. After excavation, the samples were isolated in anoxic conditions in order to limit drying and oxidation processes: they were placed in air and water tight plastic bags (ESCAL© film, Long Life for Art, Germany) with oxygen scavenger bags (ATCO© FTM absorbers, Long Life for Art, Germany).

3. Analytical methodology

3.1. Elemental analysis

C, H, N, and S measurements were conducted on an elemental analyzer (Flash EA® 1112, Thermo Scientific, USA) based on a dynamic combustion method. Samples, 0.5 to 2 mg each, are introduced in a high temperature (1800 °C) reactor, in which they are completely conversed into gases that are afterwards analyzed by chromatography.

Iron and calcium measurements were subcontracted to the Institut des Sciences Analytiques, Villeurbanne, France. These measurements were performed by inductively coupled plasma atomic emission spectroscopy (ICP-AES, ICAP 6500, Thermofisher Scientific) after mineralization of the samples in concentrated acid.

3.2. X-ray diffraction (XRD)

3.2.1. Identification of crystalline phases

Major phases were determined on powder samples using a conventional Cu-Kα (λ = 1.5418 Å) powder diffractometer (D2 Phaser, Bruker, Germany) equipped with a Ceramic KFL X-ray tube source and a 1D-linear LynxEye detector. Spectra acquisition was performed with standard conditions: 30 kV; 10 mA; 2θ range: 3° to 65°; timescan 0.2 s·step^{-1}; 0.02° steps; angular speed of the sample

125 rad·min^{-1}. Minerals were identified using the PDF database of the Joint Committee Powder Diffraction Standard.

3.2.2. Separation and identification of the clay fraction

The clay fraction of shale show X-ray diffraction patterns at 7 Å, 10 Å and around 14 Å inter-reticular distances. These patterns are similar for a large number of clay minerals, which seriously limits their identification by a single XRD experiment. Clay minerals can however be differentiated by considering their main structural and swelling properties (sorption, hygroscopicity, deformation under various RH conditions, etc.) and by the use of conventional preparation methods (Brindley and Brown, 1980).

Clay mineral analysis involves the separation of a clay sized fraction (usually < 2 micron) from the sample, based on consecutive cleaning-centrifugation cycles. Samples were first ground in an agate mortar in order to allow for a primary detachment and dispersion of the clay mineral particles from the matrix. In the first step, 20 to 50 g of ground shale is mixed with 200 mL of distilled water and centrifuged at 2500 round·min^{-1} for 10 minutes. After removal of the supernatant, the sludge residue is mixed again with water. Centrifugation is repeated until a stable solution without flocculation of clay particles is reached. The thinnest clay mineral particles are then situated in the higher part of the supernatant. After a last centrifugation (3500 round·min^{-1} for 45 minutes), the solution is allowed to stand for 2 hours, thus provoking a gravimetric separation of the largest particles (>2 μm, Stockes' law). The clay fraction (<2 μm) is finally collected from the supernatant solution and deposited on a glass slide substrate using the Millipore® filter transfer method (Moore and Reynolds, 1997).

For each clay fraction, three samples were prepared. Those hereafter referred to as AD were simply air-dried; those hereafter referred to as EG were spread with ethylene glycol; those hereafter referred to as H were heated at 490 °C for 4 hours.

This more precise XRD analysis was not performed on the above mentioned diffractometer, but on a Co-Kα (λ = 1.789 Å) powder diffractometer (D8 Advance, Bruker, Germany) coupled with a LinxEyes 1D detector Fe-filtered radiation using the following conditions: 40 kV; 35 mA; 2θ range: 3° to 35°; timescan 1.5 s·step^{-1}; 0.02° steps; no rotation of the sample. All spectra were treated with the EVA software (Bruker, Germany).

3.3. Mössbauer spectrometry (MS)

MS measurements were performed at room temperature (293 K) with a perpendicular incident beam, using a constant acceleration HALDER type spectrometer, with a ^{57}Co source (Rh matrix) in transmission geometry. Polycrystalline absorbers containing about 10 mg·cm^{-2} of iron were used to avoid the experimental widening of the peaks. The velocity was calibrated using pure iron metal as model material.

The spectra refinement was performed in two steps. Experimental data were first resolved with symmetric doublets of Lorentzian absorption peaks using an iterative least-squares model program. This approach allows for a first determination of hyperfine experimental parameters for the different iron sites: position (δ), amplitude and width (Γ) of each peak. With this first approach, line broadening was notable, leading to a peak shape different from a Lorentzian profile. This broadening is characteristic of disordered compounds where a multiplicity of environments occurs for each iron site. This is typically the case of clays minerals where substitutions take place.

A second approach was also developed in which the spectra were modeled with quadrupolar splitting distributions according to the Hesse and Rubartsch method (Hesse and Rubartsch, 1974) and using for Γ and δ the same values as previously determined in the first refinement. This second approach allowed for a better determination of hyperfine parameters which are related to the chemical environment of iron: the isomer shift, δ, enables the determination of the oxidation state and the coordination of iron; the quadrupolar splitting, Δ, gives information on the distortion of the environment of iron, and finally, the linewidth, Γ, indicates the order-disorder state of the material.

3.4. Mercury intrusion porosimetry

Mercury intrusion porosimetry (MIP) was performed with an AutoPore IV 9500 porosimeter system (Micromeritics, USA) using a standard procedure (ASTM, 2010). Pore size distribution (PSD) was obtained on shale samples cut in small cubes of average size 1 × 1 × 0.5 cm and weighting approximately 2 g. In order to estimate repeatability and reproducibility, measurements were duplicated and average values were considered. Before analysis, all samples were conditioned in an oven at 70 °C for drying until a constant mass was reached.

Samples were submitted to a deaerating process with a residual pressure of 50 μm Hg. These conditions allow for a single-phase flow (vacuum/mercury) in the porous network. A mercury contact angle of 136° and a mercury surface tension of 485 mN·m^{-1} were considered for data treatment.

Because mercury is a no-wetting liquid, an increasing pressure of mercury is required to fill the smallest pores of the porous network according to the Laplace's law (Van Brakel et al., 1981). Pressure was therefore raised up to 206 MPa thus allowing the investigation of pore size from 180 μm to 3 nm. Such experimental conditions lead to some underestimation of the true porosity of the shale because mercury is not able to penetrate into the smallest pores of the microporosity (<3 nm), as well as into the clay particle sheets.

3.5. Permeability measurements

Water vapor permeability was measured following a standard procedure based on the "dry cup" method (AFNOR, 2010). All measurements were duplicated. Square samples of approximate dimension 35 × 35 × 2.5 mm were first polished with abrasive paper then placed for two days in a conditioned room at 23 °C and 50% relative humidity (RH). They were then sealed with butyl rubber mastic (GEB, FR) to the caps of glass containers previously filled with dry silica gel. The glass container with the shale sample was then located in a conditioned room at 23 °C and 50% RH for approximately 15 days. Temperature and humidity conditions in the glass containers was monitored with small loggers (Hygrobutton, ProgesPlus©, France) showing that dry silica gel was efficient enough to keep relative humidity below 1% all along the experiment.

The moisture gradient between the outside and the inside of the container provokes a transfer of water vapor from the outside to the inside of the container. The mass of this latter is regularly recorded thus allowing the calculation of the permeability and the water vapor resistance coefficient μ.

Air permeability was measured using the DarcyPress™ experimental setup specially developed by Cydarex (Rueil Malmaison, France) for small samples, approx. 1 cm large. The sample is embedded in a viscous polyester resin, cut in a 2 to 5 mm thick disc, polished, then placed in a core holder under a confining pressure of 10 bars for transverse permeability measurements according to a procedure already depicted elsewhere (Lenormand et al., 2010).

Table 1
Chemical and petrophysical data recorded on newly excavated material.
Données chimiques et pétrophysiques obtenues sur le materiel nouvellement prélevé sur site.

		Surmoulin	*Muse FL*	*Muse*
CHNS analysis (% w/w)	C	13 (1)	12 (1)	9 (1)
	H	1.0 (2)	2.0 (2)	1.4 (2)
	N	0.2 (2)	0.4 (2)	0.2 (2)
	S	Not detected	Detected, <0.5	Not detected
ICP-AES (% w/w)	Fe	1.8 (1)	1.5 (1)	1.8 (1)
	Ca	7.6 (1)	0.3 (1)	0.3 (1)
X-ray diffraction, bulk analysis	Pyrite		x	
	Plagioclase	x		
	K-Feldspar		x	x
	Quartz	x	x	x
	Kaolinite	x	x	x
	Dolomite	x		
X-ray diffraction, clay fraction	Illite	x (not pure)	x	x
	Kaolinite	x	x	x
	Vermiculite	x (interstratified)	x	
Water vapor resistance Coefficient μ	Sample 1	358	3039	1023
	Sample 2	234	3066	2105
Mercury intrusion porosimetry	Total open porosity (v/v)	9.8%	8.2%	6.9%
	Pore radius (open porosity)	~7 nm (7.4%)	~7 nm (7.4%)	~3 nm (5.5%)
		~150 nm (2.0%)		
		>250 nm (0.4%)	>250 nm (0.8%)	>250 nm (1.4%)

4. Results

4.1. Elemental analyses

Elemental measurements (Table 1) show that shale samples contain significant amounts of carbon (9 to 13% w/w), some amount of iron (1 to 2% w/w) and hydrogen (1 to 2% w/w). Nitrogen is also present, but in smaller amount (0.2 to 0.4% w/w).

Calcium was detected in all samples, yet in varying quantities (0.3% w/w for *Muse, Muse FL* and 7.6% w/w for *Surmoulin*). On the contrary, no sulfur was detected in the samples of *Surmoulin* and *Muse*, and some minor amount of sulfur was evidenced in the *Muse FL* sample (although it was not possible to quantify it). This means that the concentration of sulfur is below or in the range of the detection limit of the apparatus (estimated to be close to 0.2–0.3% w/w).

4.2. XRD

Shale samples of *Muse*, *Muse FL* and *Surmoulin* (Fig. 3 and Table 1, XRD, bulk analysis) contain quartz, K-feldspar or plagioclase and clay minerals (peaks at 7 Å, 10 Å and 14 Å). Dolomite was additionally detected in the *Surmoulin* sample. Pyrite was expected in all samples but was found as a diffracting material in *Muse FL* only.

Specimens 6889, 6891 and 6892 show similar features as *Muse*, *Muse FL* and *Surmoulin*, yet they do not show any signal corresponding to dolomite or plagioclase. Cristallized iron oxides, often associated to weathering by-products, were not detected. Degradation ancillary products could also be related to iron sulfates resulting from sulfide oxidation. Jarosite ($KFe^{III}_3(OH)_6(SO_4)_2$) was identified on specimen 6889, but no iron sulfate was detected in newly excavated shale samples.

The clay fractions showed d(001) characteristic peaks at 7 Å, 10 Å and 14 Å (Fig. 4) which were attributed to different types of clay minerals (Table 1, XRD, clay fraction), taking into account the following arguments: (i) On all samples, the peak at 7 Å remains unchanged after ethylene glycol treatment (EG) and disappears after heating (H), which is consistent with the behavior of kaolinite. Also the samples do not contain any chlorite; (ii) On all samples, the peak at 10 Å remains at the same position after ethylene glycol (EG) or heating (H) treatments. This behavior is characteristic of illite. In the case of *Surmoulin*, this peak is highly asymmetric, meaning that illite is partly open. (iii) On the samples of *Muse FL*, the peak at 14 Å remains unchanged after ethylene glycol (EG) treatment and is shifted to 10 Å after heating (H). This behavior is characteristic of vermiculite. (iv) on the sample of *Surmoulin*, the peak at 14 Å is shifted to 15.5 Å after ethylene glycol (EG) treatment and to lower values (10 to 14 Å) after heating (H). This indicates the presence of swelling clay minerals. This behavior however does not match with pure vermiculite. It more probably corresponds to interstratified vermiculite based clays.

4.3. Mössbauer spectroscopy

MS spectra were satisfactorily modeled with quadrupole-split doublets distributions (Fig. 5), leading to the detection of three to four sites of similar MS parameters in each sample (Table 2). Octahedral high spin Fe(II) (δ between 1.05 and 1.14 $mm{\cdot}s^{-1}$ and Δ between 2.57 and 2.72 $mm{\cdot}s^{-1}$) is present in all samples, as octahedral high spin Fe(III) (Fig. 6). This latter is often distributed in two sites (Table 2): the first shows an isomer shift value in the range 0.4 to 0.45 $mm{\cdot}s^{-1}$ and a relatively high quadrupolar splitting in the range 0.92 to 1.28 $mm{\cdot}s^{-1}$; the second shows a lower isomer shift value in the range 0.3 to 0.39 $mm{\cdot}s^{-1}$ and a lower quadrupolar splitting in the range 0.66 to 0.96 $mm{\cdot}s^{-1}$.

A special attention was paid to the MS signature of pyrite that corresponds to an isomer shift of approx. 0.30 $mm{\cdot}s^{-1}$ and a quadrupolar splitting of approx. 0.6 $mm{\cdot}s^{-1}$ (Stevens et al., 2005) (Fig. 6). This signature, found in the two samples *Muse* and *Muse FL*, will be discussed below in more details.

4.4. Porosimetry

The measured values of shale open porosity range from 7 to 10% v/v (Table 1, Mercury intrusion porosimetry). Measurements were duplicated on each shale materials and reproducible PSD were obtained, thus enabling a satisfactory description of the shale microstructural features. *Muse FL* and *Muse* samples show respectively a 7 nm and 3 nm centered unimodal PSD. Such dimensions are consistent with the pore space between mineral grains, including clay particles. *Surmoulin* samples show a bimodal PSD with a main representative mode situated at 7 nm (consistent with

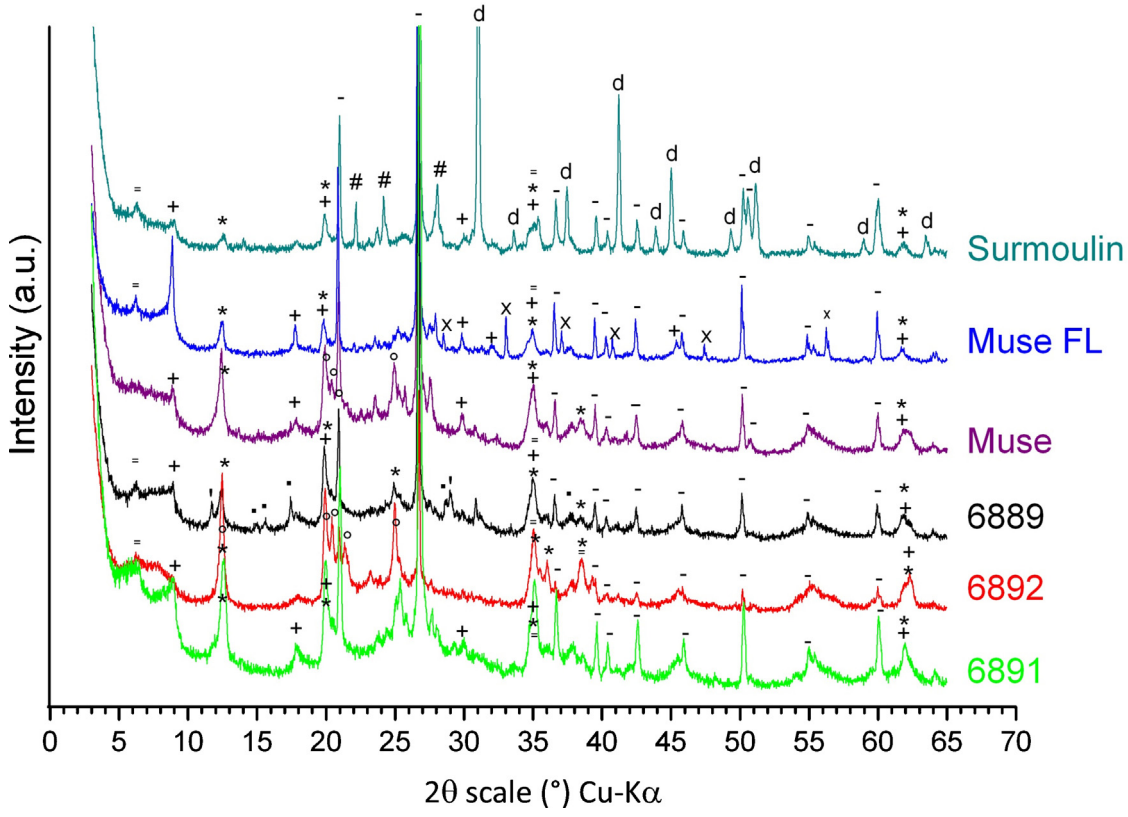

Fig. 3. X-ray diffraction patterns of shale samples (bulk analysis). Peak assignment: quartz (-), jarosite (■), pyrite (x), plagioclase (#), K-feldspar (o), gypsum ('), kaolinite (*), dolomite (d), illite (+), vermiculite (=).
Profils de diffraction des rayons X des schistes argileux (analyse de matrice). Attribution des pics : quartz (-), jarosite (■), pyrite (x), plagioclase (#), feldspath K (o), gypse ('), kaolinite (*), dolomite (d), illite (+), vermiculite (=).

the space between mineral particles) and a second well defined mode, situated around 150 nm, that is related to opened pores, revealing both the bedding and cleavage of shale.

In addition, a small amount of larger pores ranging from 0.2 to 100 microns is detected on the *Muse* samples (Fig. 7c). These macropores are sometimes visible to the naked eye on the surface of the samples. However, they are not numerous enough to significantly increase the shale open porosity that remains, in the case of *Muse* samples, at a low value of 6.9% v/v.

4.5. Permeability measurements

The water vapor diffusion resistance μ significantly differs from one shale sample to another (Table 1, water vapor resistance coefficient μ). *Muse FL* samples were highly impermeable, with μ values close to 3050. *Muse* has lower μ values in the order of 1000–2000. *Surmoulin* appears relatively more permeable, with μ values in the order of 200–400.

For apparatus availability reasons, transverse air permeability measurements were performed on *Muse FL* samples only. The measurements showed that the air flow in the porous network was extremely low regarding to the small dimension of the sample (2 millimeters thick) and to the high pressure that is applied (10 bars). Whilst permeability test on rock samples (granite, sandstone or limestone) is generally achieved in few minutes, it was necessary to wait for about 4 hours before detecting a small variation of the downstream pressure below the sample. Assuming that the Darcy flow law is still valid in these conditions, permeability values in the order of a few nano Darcy were calculated. *Muse FL* sample can therefore be considered as impermeable to air.

5. Discussion

5.1. Questioning the occurrence of iron sulfide

5.1.1. Newly excavated shale samples

Elemental measurements show that the amount of iron present in newly excavated shale samples is above 1.5% w/w whereas the amount of sulfur is below 0.5% w/w on *Muse FL* sample and below 0.2–0.3% w/w on *Muse* and *Surmoulin* samples. Such a difference means that iron sulfide, if present, involves a minor proportion of iron. Pyrite (FeS_2) is surely present in *Muse FL* shale as it was detected by XRD, but its occurrence is seriously questionable in *Muse* and *Surmoulin* samples.

MS measurements complementary highlight this point. High resolution MS data available in the literature (Stevens et al., 2005) show that pyrite has a well-defined MS signature of low spin Fe(II), with an isomer shift in the range 0.30 to 0.32 $mm{\cdot}s^{-1}$ and a quadrupolar splitting in the range 0.60 to 0.62 $mm{\cdot}s^{-1}$ (Fig. 6). The *Muse FL* sample, in which pyrite was detected by XRD, shows a signature ($\delta = 0.30\ mm{\cdot}s^{-1}$, $\Delta = 0.68\ mm{\cdot}s^{-1}$) that is very close to these data. It also, at least partly, corresponds to pyrite. The *Muse* sample shows a similar signature ($\delta = 0.31\ mm{\cdot}s^{-1}$, $\Delta = 0.69\ mm{\cdot}s^{-1}$) that could be as well attributed to some proportion of iron sulfide. This iron sulfide would then be poorly crystallized or crystallized on a nanoscale, since it is not detected by XRD. Unlike the *Muse* and *Muse FL* samples, the *Surmoulin* sample shows no MS signatures that could be attributed to pyrite (values of δ above 0.39 $mm{\cdot}s^{-1}$ and values of Δ above 0.87 $mm{\cdot}s^{-1}$).

There are many other types of iron sulfides, such as marcasite (a pyrite polymorph) or "FeS" type sulfides (pyrrhotite, troilite, mackinawite, etc.) that could as well enter into the composition

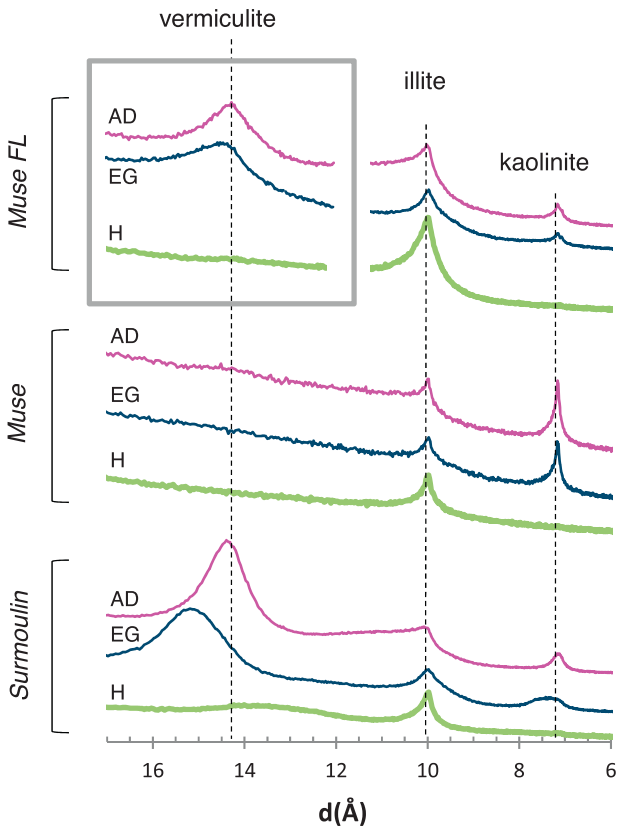

Fig. 4. X-ray diffraction patterns of isolated clay fractions. Muse FL (top); Muse (middle); Surmoulin (bottom); after drying (AD); treated with ethylene glycol (EG); heated at 490 °C (H).
Profils de diffraction des rayons X des fractions argileuses isolées. Muse FL (haut) ; Muse (milieu) ; Surmoulin (bas) ; après séchage (AD) ; traité à l'ethylène glycol (EG) ; chauffé à 490 °C (H).

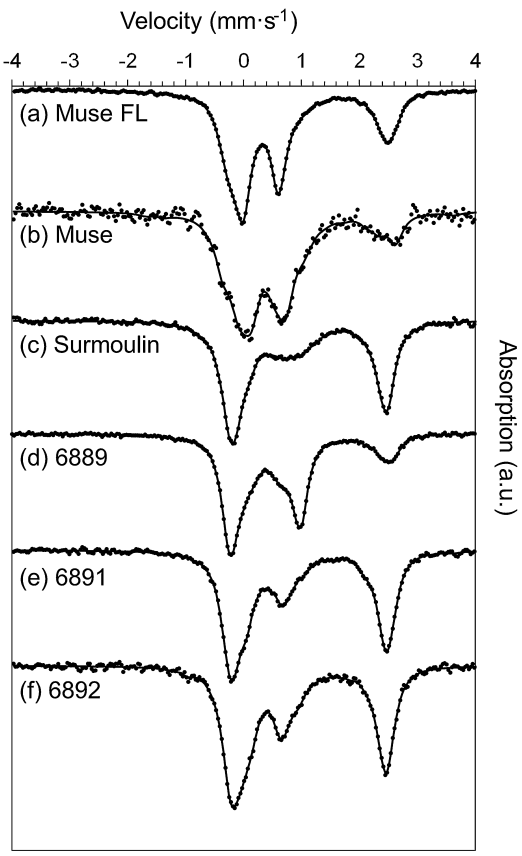

Fig. 5. Mössbauer spectra recorded on shale samples. Measurements (dots) and quadrupole-split doublet distributions (line) of samples Muse FL (a), Muse (b), Surmoulin (c) and shale fraction of specimen 6889 (d), 6891 (e) and 6892 (f).
Spectres Mössbauer des échantillons de schistes argileux. Mesures (pointillés) et calculs en distribution quadrupolaire (ligne) des échantillons Muse FL (a), Muse (b), Surmoulin (c) et des prélèvements de schistes réalisés sur les spécimens 6889 (d), 6891 (e) et 6892 (f).

Table 2
Mössbauer parameters measured on shale samples with tentative attributions. Isomer shift (δ), quadrupolar splitting (Δ) and linewidth (Γ) are expressed in mm·s^{-1}. The quotation $^{(6)}$Fe corresponds to octahedral iron sites.
Paramètres Mössbauer mesurés sur les écahntillons de schistes argileux avec leur essai d'attribution. Déplacement isomérique (δ), éclatement quadrupolaire (Δ) et largeur de raie (Γ) sont exprimés en mm·s^{-1}. La notation $^{(6)}$Fe correspond à un site octahédrique de fer.

Samples	δ	Δ	Γ	%		Interpretation
Surmoulin	1.13	2.62	0.2	58	$^{(6)}Fe^{2+}$	Clay
	0.39	0.87	0.3	25	$^{(6)}Fe^{3+}$	Clay
	0.42	1.28	0.3	17	$^{(6)}Fe^{3+}$	Clay
Muse	1.13	2.72	0.3	24	$^{(6)}Fe^{2+}$	Clay
	0.4	0.87	0.3	45	$^{(6)}Fe^{3+}$	Clay
	0.31	0.69	0.3	31	$^{(6)}Fe^{2+}$ low spin, $^{(6)}Fe^{3+}$	Possibly pyrite and/or clay
Muse FL	1.13	2.68	0.25	41	$^{(6)}Fe^{2+}$	Clay
	0.4	1.15	0.3	7	$^{(6)}Fe^{3+}$	Clay
	0.3	0.68	0.25	52	$^{(6)}Fe^{2+}$ low spin, $^{(6)}Fe^{3+}$	Pyrite (detected by XRD) and possibly clay
6889	1.14	2.64	0.2	13	$^{(6)}Fe^{2+}$	Clay
	1.05	2.57	0.2	11	$^{(6)}Fe^{2+}$	Clay
	0.33	0.96	0.2	40	$^{(6)}Fe^{3+}$	Clay
	0.42	1.11	0.2	36	$^{(6)}Fe^{3+}$	Jarosite (detected by XRD) and possibly clay
6891	1.123	2.66	0.25	63	$^{(6)}Fe^{2+}$	Clay
	0.452	0.92	0.25	11	$^{(6)}Fe^{3+}$	Possibly clay and/or Fe^{3+} sulfate
	0.363	0.76	0.25	26	$^{(6)}Fe^{3+}$	Clay
6892	1.123	2.61	0.25	55	$^{(6)}Fe^{2+}$	Clay
	0.452	1.17	0.25	16	$^{(6)}Fe^{3+}$	Possibly clay and/or Fe^{3+} sulfate
	0.363	0.66	0.25	29	$^{(6)}Fe^{2+}$ low spin, $^{(6)}Fe^{3+}$	Pyrite (S K-edge XANES) and possibly clay

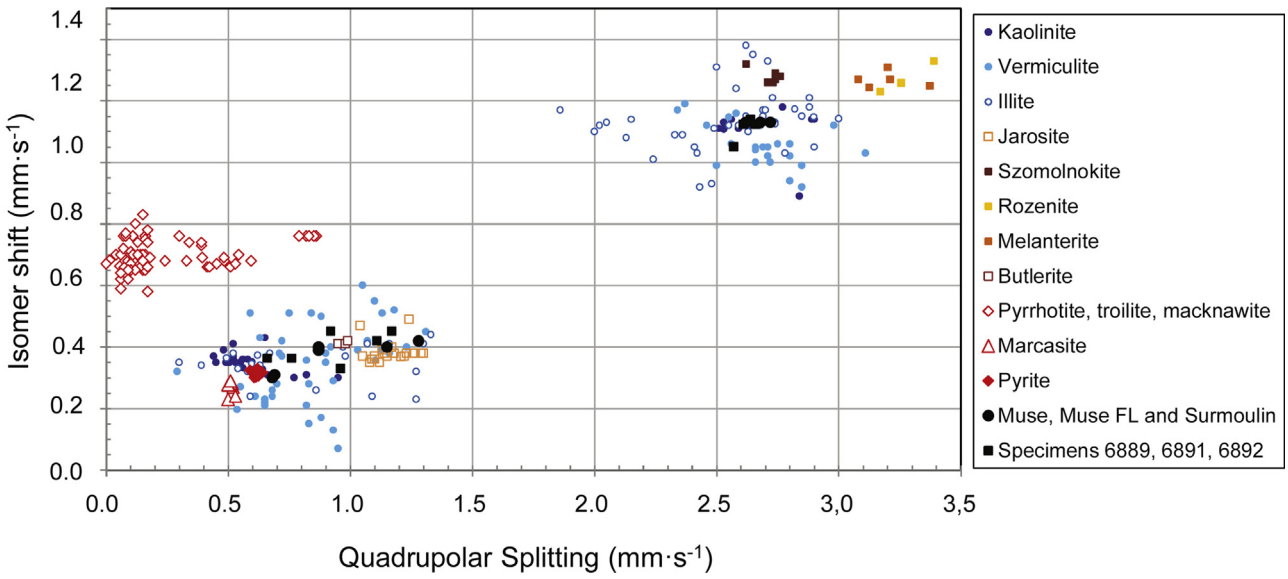

Fig. 6. Mössbauer parameters measured on shale samples and collected in the literature. List of references (Dyar et al., 2013; Ferrow, 2002; Huffman and Huggins, 1978; Loayza et al., 2011; Medina et al., 2006; Olowe and Genin, 1991; Pysh'yev et al., 2004; Saint Pierre et al., 1992; Stevens et al., 2005; Verma and Tripathi, 2000; Wagner and Wagner, 2004).
Paramètres Mössbauer mesurés sur les échantillons de schistes argileux et trouvés dans la littérature. Liste des références (Dyar et al., 2013 ; Ferrow, 2002 ; Huffman et Huggins, 1978 ; Loayza et al., 2011 ; Medina et al., 2006 ; Olowe et Genin, 1991 ; Pysh'yev et al., 2004 ; Saint Pierre et al., 1992 ; Stevens et al., 2005 ; Verma et Tripathi, 2000 ; Wagner et Wagner, 2004).

of shale. None of them was detected by XRD. Moreover, their MS parameters significantly differ from those measured on our samples (Fig. 6). The occurrence of other types of iron sulfides appears also unlikely.

Considering these observations, it can be concluded that *Surmoulin* samples contain no significant amount of iron sulfide, that *Muse* probably contains some nanoscale or poorly crystallized pyrite and that *Muse FL* samples show some proportion of iron (below 52%) under the form of pyrite.

5.1.2. Shale fraction of MNHN specimens

The specimens 6889, 6891 and 6892 are expected to originally have contained some pyrite. Yet they were collected in the 19th century and were thus exposed to air for more than one century. Pyrite, if initially present, is then supposed to be largely oxidized. This point was confirmed in a previous work by S K-edge XANES measurements showing that sulfur was dominantly under the form of sulfates (Odin et al., 2014). As a result, no MS signature of iron sulfide is detected in the specimens 6889 and 6891. Yet, on the specimen 6892, the Mössbauer site of isomer shift 0.363 $mm{\cdot}s^{-1}$ and quadrupolar splitting 0.66 $mm{\cdot}s^{-1}$ appears to us at least partially correlated to pyrite (Table 2) consistent with the fact that minor traces of iron sulfide (FeS_2) were in a previous work highlighted on this specimen (fig. 5 of Odin et al., 2014).

5.2. The speciation of iron in shale

Iron may be related to iron sulfide (see above), clays minerals, iron sulfate (jarosite was evidenced by XRD in specimen 6889) or iron oxyhydroxides as weathering products.

Several Mössbauer spectroscopy studies were dedicated to clay minerals (Ferrow, 2002; Loayza et al., 2011; Medina et al., 2006; Murad, 1998; Ruby et al., 1999; Saint Pierre et al., 1992; Stevens et al., 2005; Wagner and Wagner, 2004) showing a large dispersion and overlapping of MS signatures (Fig. 6). These studies highlight several features regarding the distribution of iron in clay minerals. Firstly, Fe(II) is too large in tetrahedral configuration to substitute for Al. It is also present in octahedral coordination only whereas Fe(III) may be present in octahedral configuration or tetrahedral configuration. Secondly, depending on the location of OH in the octahedra, two iron configurations can be distinguished: cis (M2) in which the hydroxyls are adjacent and trans (M1) in which they occupy opposite corner of the octahedra. It is also theoretically possible to detect five different MS signatures. Yet, experimental data related to clay minerals generally refer to 2 to 4 sites for the following reasons. Firstly, iron does not necessarily occupy all possible sites. For instance only illites that are specifically rich in iron may contain tetrahedral Fe(III) (Murad, 2010). Secondly, a large broadening of resonant lines is often observed, caused by isomorphous substitutions taking place in both the octahedra and tetrahedra sites. As a result of this broadening, it is often impossible to assign the M1 or M2 site by MS spectroscopy (Michael and McWhinnie, 1989; Murad, 1998).

The clay fractions (<2 μm) of *Muse, Muse FL* and *Surmoulin* contain some proportions of iron as confirmed by elemental analysis performed on a scanning electron microscope equipped for energy dispersive X-ray spectroscopy (not shown). XRD measurements highlighted the presence of illite and vermiculite, two clay minerals that often include some proportion of iron. Kaolinite was also highlighted. It is reported that this clay may contain some amount of iron (Murad, 2010; Saint Pierre et al., 1992; Stevens et al., 2005). Yet, this amount remains low as the substitution of Al by Fe is weak (<2%) to nil (Murad, 1998) whereas illite already contains from 1% to 8% of iron (Murad, 1998). The amount of iron detected in the clay fractions is also more likely related to illite or vermiculite.

MS measurements are in good agreement with these general considerations. Fe(III) sites exclusively correspond to octahedral configurations. In most cases, their MS parameters are in good agreement with those of illite and vermiculite and slightly shifted toward higher values of quadrupolar splitting with respect of those of kaolinite (Fig. 6). This confirms that the kaolinite present in the samples does not contain Fe(III).

All samples contain a significant proportion of octahedral Fe(II) (24 to 63%) with isomer shift values ranging from 1.12 to 1.14 $mm{\cdot}s^{-1}$ and quadrupolar splitting values ranging from 2.61 to 2.72 $mm{\cdot}s^{-1}$. These values are in good agreement with those of clays minerals and significantly differ from those of Fe(II) sulfates (szomolnokite, rozenite and melanterite show isomer shift values

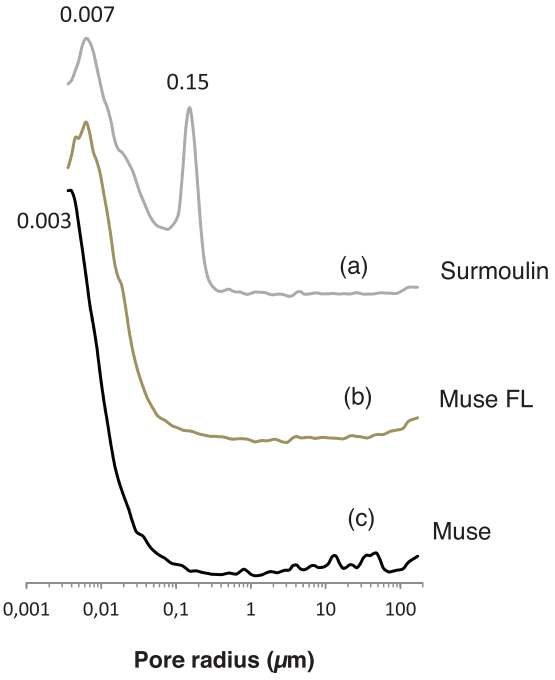

Fig. 7. Pore distribution (radius) measured by mercury intrusion porosimetry on Surmoulin (a), Muse FL (b) and Muse (c) shale.
Distribution de pores (rayon) mesurée par porosimétrie au mercure sur les schistes argileux Surmoulin (a), Muse FL (b) et Muse (c).

in the range 1.23 to 1.32 mm·s^{-1}) (Fig. 6). Fe(II) sites are thus unambiguously attributed to clay minerals (Table 2).

The MS parameters of jarosite, one of the most common Fe(III) sulfates, are in the range 0.35 to 0.40 mm·s^{-1} for δ and 1.05 to 1.2 mm·s^{-1} for Δ. Those of butlerite are close to 0.4 mm·s^{-1} for δ and 1.0 mm·s^{-1} for Δ. These values largely superimpose those of vermiculite and illite. It is also not possible to distinguish these different phases by MS spectrometry only. In some cases, XRD measurements give more conclusive answers: for instance, it confirmed the presence of jarosite in sample 6889 (Fig. 3). However, Fe(III) sulfates could be as well present under a poorly crystallized form or under nanoscale crystals that would thus not be detected by XRD. This may happen in the two specimens 6892 and 6891 that respectively exhibit Fe(III) sites with MS parameters close to those of jarosite and butlerite. This hypothesis is rather appealing as Fe(III) sulfates are expected in the three specimens 6889, 6891 and 6892. Indeed, previous S K-edge XANES analysis (Odin et al., 2014) showed an almost complete oxidation of sulfides to sulfates. These sulfates are possibly bound to iron or calcium (gypsum as well is detected by XRD in specimen 6889).

On the contrary, the presence of sulfates in *Muse*, *Muse F*L, and *Surmoulin* shale samples appears relatively unlikely for two reasons: firstly, these samples were kept apart from oxygen between their collection and their analysis; secondly S K-Edge XANES analysis (Odin et al., 2015) performed on similar samples confirmed that sulfur speciation was almost exclusively corresponding to sulfides.

The occurrence of Fe(III) oxyhydroxides in shale is often mentioned in the literature as weathering products (Murad, 1998). In this study, none of these compounds are detected by XRD, which does not rule out their presence under a poorly crystallized form. MS enables the characterization of amorphous phases and thus gives some additional information. No magnetic field was detected in the samples at ambient temperature, meaning that there are no magnetically ordered Fe(III) oxyhydroxides such as maghemite, magnetite, hematite and goetite.

Not all Fe(III) oxyhydroxides are magnetically ordered at room temperature. In particular lepidocrocite, akaganeite and ferrihydrite, three common oxyhydroxides exhibit no magnetic field at ambient temperature. Lepidocrocite and akaganeite show quadrupolar splitting values below 0.55 mm·s^{-1} (Murad, 1998; Stevens et al., 2005) that significantly differ from those measured on shale samples. Their presence also appears unlikely. On the contrary, ferrihydrite exhibits several Fe(III) sites showing similar isomer shift (0.35 mm·s^{-1}) and quadrupolar splitting values ranging from 0.5 mm·s^{-1} to 1 mm·s^{-1} (Murad and Schwertmann, 1980). These values are in the same range as those measured on specimens 6891 and 6892. The presence of ferrihydrite cannot be ruled out, but appears relatively uncertain to us for another reason: the proportion of Fe(II) in newly excavated shale and original specimens 6889, 6891 and 6892 is comparable, meaning that Fe(II) originally present in shale is not drastically oxidized despite the long term exposure of shale to oxygen. This point will be further discussed below with respect to permeability measurements.

5.3. Porosity and water vapor permeability measurements

Porosity measurements are in good agreement with water vapor permeability measurements. *Muse FL* samples show a low open porosity (7.4%) with a nanoscale unimodal pore size distribution around 7 nm. This is consistent with their high resistance to vapor diffusion (~3050) and insignificant air permeability.

The open porosity of *Muse* samples is lower (5.6% v/v) and mainly corresponds to narrower pores (3 nm). Yet *Muse* samples additionally show a minor proportion of macro-pores (Fig. 7). The connectivity of macro-pores within the pores network greatly facilitates the transfer of water vapor through the porous media. This may explain the high dispersion of water vapor resistance coefficient measurements (1023 and 2105) and the higher permeability of *Muse* samples compared to *Muse FL* samples.

The *Surmoulin* samples show the highest value of porosity (9.8% v/v) consistent with the fact that their water vapor resistance coefficient is relatively low (230–360) in comparison to the *Muse* and *Muse FL* samples. Last but not least, the poral mode around 150 nm, characteristic of the *Surmoulin* samples, enhances the network connectivity and thus certainly plays a major role in water vapor transfer.

5.4. Connecting iron speciation to permeability measurements

Shale samples chosen for this study were collected near to the surface, close to areas showing rusty deposits. They were however selected for their black aspect and the absence of obvious signs of weathering.

Shale ability to be weathering-prone is directly connected to the porosity of the material and its permeability to water and oxygen. Oxidation of iron sulfides into iron sulfates can occur with water only or oxygen only even if it is drastically enhanced by a combination of both (Rosso and Vaughan, 2006). It has been shown that newly excavated shale samples were certainly poorly permeable to water vapor, but still permeable, meaning that water vapor can migrate transversally through sedimentary layers and oxidize pyrite grains located near the porous network. The kinetic of this oxidation is probably low (pyrite traces are still detected in specimen 6892 although it was collected in the 19th century). We suppose that this low kinetic is correlated to migration phenomena favored by moisture gradients. However, sulfide oxidation occurs at least on the scale of a century, leading for instance to the formation of jarosite in specimen 6889 (XRD and MS measurements).

Unlike sulfates, Fe(III) oxyhydroxides are formed with combined interaction of iron, water and oxygen. Yet it has been shown that *Muse FL* was totally impermeable to air, meaning that oxygen does

not penetrate across the material. It also does not access iron. This is to our opinion the reason why the presence of oxyhydroxides is very unlikely in the *Muse FL* sample, despite the fact that it was collected near to areas showing obvious iron oxidation products. These oxidation products form in the cleavage plans that are accessible to liquid water and dissolved oxygen, but they do not form in the shale itself as this latter is impermeable to oxygen.

6. Conclusion

This work was undertaken in order to characterize Autunian shale with a specific attention paid to iron speciation. MS was used complementary to XRD analysis for the characterization of poorly diffracting phases. The combined use of these two techniques show that the *Surmoulin* shale is pyrite free whereas *Muse* and *Muse FL* shale contain some pyrite, yet in low amount (below 1% w/w).

It additionally shows that the major part of iron is bound to clay minerals, with a great proportion of Fe(II). This proportion is not affected by long term exposure to ambient conditions suggesting that Fe(II) sites are poorly reactive during weathering phenomena. This aspect is confirmed by permeability measurements. *Muse FL* shale is poorly permeable to water vapor and almost fully impermeable to oxygen, meaning that water vapor can slowly access the porous network whereas oxygen cannot. The combination of oxygen and water, that is necessary for Fe(II) oxidation, can thus not occur in the inner part of shale. It however happens on site in cleavage plans that are accessible to liquid water and dissolved oxygen.

Pyrite can oxidize by exposure to water only. This reaction is rather limited in comparison to combined water and oxygen exposure, but still happens. It leads to the formation of a low amount of iron sulfate in the inner part of shale, which is typically related to weathering phenomena. Due to the low amount of pyrite, this weathering cannot be considered as strong damage: iron sulfate remains distributed on a micro-nanoscale in the inner part of shale and does not affect appearance and integrity of the material.

This work shows that iron present in shale has a limited reactivity that can certainly not account for the growth of iron sulfate efflorescence observed at the surface of shale specimens. These damaging phenomena probably occur locally on specific spots that contain reactive species, the nature of which is still unknown. They do not involve transport phenomena from the inner to the outer part of shale. This work will also be pursued with the investigation of sulfur speciation in the proximity of fossil shape.

Disclosure of interest

The authors declare that they have no conflict of interest concerning this article.

Acknowledgements

This work was conducted within a PhD work that was supported by a doctoral school grant of the Muséum national d'Histoire naturelle, Paris, France. It also corresponds to a Master thesis supported by the Labex Patrima, Fondation des Sciences du Patrimoine. We are particularly grateful to M. Roland Lenormand (Cydarex, Rueil-Malmaison, France) who kindly performed air permeability tests. This work was realized in partnership with the Palaeontological Collection Management Unit, Collection Department, National Museum of Natural History (Paris, France). We also would like to thank MM. Hervé Lelièvre, Olivier Bethoux, Sebastien Steyer, Jean Dejax, Dario de Franceschi and Marie Madeleine Blanc Valleron for their advice and assistance.

References

AFNOR, 2010. NF EN 15803, conservation des biens culturels : méthodes d'essai - Détermination de la perméabilité à la vapeur d'eau.
Brindley, G.W., Brown, G.E., 1980. Crystal structures of clay minerals and their X-ray identification, vol. 5. Mineralogical Society monograph, London.
Chateauneuf, J.J., Farjanel, G., Feys, R., Marteau, P., 1980. Sondages stratigraphiques dans le bassin d'Autun : étude préliminaire. Bulletin trimestriel de la Société d'Histoire Naturelle et des Amis du Musée d'Autun 95, 61–83.
Dyar, M.D., Breves, E., Jawin, E., Marchand, G., Nelms, M., O'Connor, V., Peel, S., Rothstein, Y., Sklute, E.C., Lane, M.D., Bishop, J.L., Mertzman, S.A., 2013. Mössbauer parameters of iron in sulfate minerals. American Mineralogist 98, 1943–1965.
Elsass Damon, F., 1977. Les "schistes bitumineux" du bassin d'Autun : pétrographie, minéralogie, cristallochimie, pyrolise. Université Pierre et Marie Curie, Paris [unpublished PhD thesis].
Ferrow, E.A., 2002. Experimental weathering of biotite, muscovite and vermiculite: a Mössbauer spectroscopy study. Eur J Mineralogy 14, 85–95.
Gand, G., Steyer, J.-S., Chabard, D., 2010. Reprise de fouilles paléontologiques dans un gîte bourguignon célèbre : les "schistes bitumineux" de l'Autunien de Muse (Bassin d'Autun). Bourgogne Nature 12, 10–28.
Hesse, J., Rubartsch, A., 1974. Model independent evaluation of overlapped Mössbauer spectra. Journal of Physics E-Scientific Instruments 7, 526–532.
Howie, F.M.P., 1977. Pyrite and conservation, part 2. Geological Curators Group Newsletter 10, 497–512.
Huffman, G.P., Huggins, F.E., 1978. Mössbauer studies of coal and coke-quantitative phase identification and direct deterlmination of pyritic and iron sulfide sulfur content. Fuel 57, 592–604.
Jambor, J.L., Nordstrom, D.K., Alpers, C.N., 2000. Metal-sulfate salts from sulfide mineral oxidation. In: Jambor, J.L., Nordstrom, D.K., Alpers, C.N. (Eds.), Sulfate Minerals: crystallography, geochemistry, and environmental significance. Mineralogical Society of America, pp. 305–350.
Lenormand, R., Bauget, F., Ringot, G., 2010. Permeability measurements on small rock samples. In: Proceedings of International Symposium of the Society of Core Analysts, Halifax 2010, A073.
Loayza, M.L.C., Cabrejos, J.A.B., Santillan, M.E.M., 2011. Mineralogy of the clay fraction of soils from the moray cusco archaeological site: a study by energy dispersive X-ray fluorescence, X-ray diffractometry and Mössbauer spectroscopy. Hyperfine Interactions 203, 133–141.
Marteau, P., 1983. Le bassin permo-carbonifère d'Autun : stratigraphie, sédimentologie et aspects structuraux. Université de Dijon [unpublished PhD thesis].
Medina, G., Tabares, J.A., Alcazar, G.A.P., Barraza, J.M., 2006. A methodology to evaluate coal ash content using Siderite Mössbauer spectral area. Fuel 85, 871–873.
Michael, P.J., McWhinnie, W.R., 1989. Mössbauer and ESR Studies of the Thermochemistry of Illite and Montmorillonite. Polyhedron 8, 2709–2718.
Moore, D.M., Reynolds, R.C., 1997. X-ray diffraction and the identification and analysis of clay minerals, 2nd edition. Oxford University Press, New York.
Murad, E., 1998. Clays and clay minerals: What can Mössbauer spectroscopy do to help understand them? Hyperfine Interactions 117, 39–70.
Murad, E., 2010. Mössbauer spectroscopy of clays, soils and their mineral constituents. Clay Minerals 45, 413–430.
Murad, E., Schwertmann, U., 1980. The Mössbauer spectrum of ferrihydrite and its relations to those of other iron oxides. American Mineralogist 65, 1044–1049.
Odin, G.P., Vanmeert, F., Farges, F., Vantelon, D., Janssens, K., Rouchon, V., 2015. Alteration of fossil-bearing shale (Autun, France, Permian), part II: monitoring artificial and natural ageing by combined use of S and Ca K-edge XANES analysis, Rock-Eval pyrolysis and FTIR analysis. Annales de Paléontologie. [In press].
Odin, G.P., Vanmeert, F., Janssens, K., Lelièvre, H., Mertz, J.-D., Rouchon, V., 2014. Accelerated ageing of shales of palaeontological interest: Impact of temperature conditions. Annales de Paléontologie 100, 137–149.
Olowe, A.A., Genin, J.M.R., 1991. Hyperfine structures of iron(II) sulfates-melanterite and rozenite. Hyperfine Interactions 68, 253–256.
Pysh'yev, S.V., Gayvanovych, V.I., Pattek-Janczyk, A., Stanek, J., 2004. Oxidative desulphurisation of sulphur-rich coal. Fuel 83, 1117–1122.
Rosso, K.M., Vaughan, D.J., 2006. Reactivity of sulfide mineral surfaces. In: Vaughan, D.J. (Ed.), Reviews in mineralogy and geochemistry: Sulfide Mineralogy and Geochemistry. Mineralogical Society of America, pp. 557–607.
Rouchon, V., Badet, H., Belhadj, O., Bonnerot, O., Lavédrine, B., Michard, J.G., Miska, S., 2012. Raman and FTIR spectroscopy applied to the conservation report of paleontological collections: identification of Raman and FTIR signatures of several iron sulfate species such as ferrinatrite and sideronatrite. Journal of Raman Spectroscopy 43, 1265–1274.
Ruby, C., Refait, P., Genin, J.M.R., Delineau, T., Yvon, J., 1999. Evidence of structural Fe(II) ions in Font-Bouillant kaolinites: a Mössbauer study. Clay Minerals 34, 515–518.
Saint Pierre, T.G., Singh, B., Webb, J., Gilkes, B., 1992. Mössbauer spectra of soil Kaolins from South Western Australia. Clays and Clay Minerals 40, 341–346.
Stevens, J.G., Khasanov, A.M., Miller, J.W., Pollak, H., Li, Z., 2005. Mössbauer Mineral Handbook. Mössbauer Effect Data Center, Asheville.
Van Brakel, J., Modry, S., Svata, M., 1981. Mercury porosimetry: state of the art. Powder Technology 29, 1–12.
Verma, H.C., Tripathi, R.P., 2000. Characterization of iron-bearing minerals in Giril lignite from Rajasthan and study of their decomposition during combustion using Fe-57 Mössbauer spectroscopy. Fuel 79, 599–606.
Wagner, F.E., Wagner, U., 2004. Mössbauer spectra of clays and ceramics. Hyperfine Interactions 154, 35–82.